S.T. Yau High School Science Award

Research Report

The Team

Name of team member: Melvin Qiu
School: Princeton High School
City, Country: Princeton, New Jersey, United States
Instructor: Siming Huang

Title of Research Report

Behavior of Geosynthetic Reinforced Soil Structures in Martian Simulant: A Pioneering Experimental and Analytical Study

Date

August 23, 2025

Behavior of Geosynthetic Reinforced Soil Structures in Martian Simulant: A Pioneering Experimental and Analytical Study

Melvin Qiu[1]
[1]Princeton High School, melvinhkq@gmail.com

Abstract: Due to the unique properties of Martian soil and hostile environmental conditions, the development of stable foundations and other geotechnical structures on Mars is essential for future human habitation. This study evaluates the effectiveness of geogrid reinforcement in a custom-prepared Martian Bright Eroded Mantle (BEM) soil simulant with physical models adapted from geosynthetic reinforced soil (GRS) abutment model setups. Geogrid spacing and material stiffness were varied independently. Displacement behavior was measured by laser displacement sensors and the ultimate bearing capacity was compared against Federal Highway Administration (FHWA) predictions. The unreinforced model collapsed during filling, while reducing spacing to 100 mm increased capacity nearly eightfold relative to 200 mm. Higher reinforcement stiffness also improved capacity, from ~80 N with glass-fiber to ~180 N with acrylic geogrids, though gains diminished at the highest stiffness. Failure consistently occurred by wall–soil wedge sliding, with geogrids bending instead of rupturing, showing that flexural resistance, rather than tensile strength, governed performance. A new analytical model accounting for sliding and bending was created that better fits the model. This study pioneers a scalable methodology for small-scale testing of alien soil simulants, guiding future extraterrestrial geotechnical design.

Keywords: Martian soil; Geosynthetic reinforced soil; Pre-cast retaining wall; Model test; Analytical model.

Table of Contents

Abstract 1
Keywords 1
I. Introduction 2
II. Experimental Methodology 3
  2.1 Martian Soil Simulant 3
  2.2 Reinforcement Material 3
  2.3 Experimental Setup and Procedure 5
  2.4 Experimental Conditions 5
III. Experimental Results 5
  3.1 Failure Mode 5
  3.2 Effect of Reinforcement Spacing 6
  3.3 Effect of Reinforcement Material 6
  3.4 Theoretical Analysis 7
    3.4.1 Comparison with FHWA Method 7
    3.4.2 New Theoretical Model for Bearing Capacity ... 7
IV. Conclusions 9
References 10
Appendix. Supplementary Figures 11
Declaration of Academic Integrity 11

Acknowledgements

The author sincerely thanks Siming Huang for her guidance and constructive suggestions on experimental setup throughout this project.

Author Contribution Statement

This work was conceived, funded, and carried out solely by the author, who designed and executed the experiments, analyzed the results, and prepared the manuscript.

I. Introduction

Mars is widely viewed as the next frontier for human habitation. Constructing a sustainable outpost on Martian soil requires many different structures, including foundations for pressurized habitats and radiation-shielding walls, stable launch and landing pads for spacecraft, rudimentary roads for mobility, and retaining structures to stabilize loose terrain. [1]. However, the construction of these structures poses immense challenges unique to Mars. These challenges stem from two major issues.

The first issue is the extreme Martian environment, which imposes increased structural loads. Large day–night temperature swings cause repeated expansion and contraction, threatening structural integrity through thermal fatigue [2]. Without a magnetic field or thick atmosphere, the surface is bombarded by cosmic and solar radiation, necessitating heavy shielding to protect astronauts and equipment [3]. The low atmospheric pressure (~0.6% of Earth's) means habitats must be fully pressurized, adding complexity to design [4]. Frequent dust storms degrade instruments and solar panels by coating or eroding material on their surfaces [5], [6], [7], [8], [9]. As a result, Martian structures must be significantly thicker, heavier, and more robust than their terrestrial counterparts, leading to greater structural loads, significant even under Mars's lower gravity.

The second issue is the unique nature of Martian soil. Generally, Martian soil is composed of fine, angular particles with high cohesion and low compaction efficiency, differing significantly from terrestrial soils [6], [10], [11], [12], [13]. These characteristics complicate construction and soil stabilization efforts on Mars.

One potential solution to improve soil performance is geosynthetic reinforcement, a technique widely used on Earth to enhance the stability and load-bearing capacity of soil structures such as retaining walls, bridge abutments, and slopes [14].

Geosynthetic reinforcements are made from high-tensile-strength materials (e.g. polypropylene, polyester, polyethylene, glass fibers, steel) and work by providing tensile resistance within the soil mass, forming a composite material that has greater shear strength and reduced deformation under load [14], [15]. Among the most widely used geosynthetics are geogrids—open, grid-like structures that interlock with surrounding soil and distribute loads over a broader area, thereby improving stability and reducing settlement [14]. Other types include geotextiles which are textile sheets, and geocomposites, which combine multiple geosynthetic types (e.g. a geogrid bonded to a geotextile) [14]. Applications span a wide range of civil infrastructure, including Mechanically Stabilized Earth (MSE) walls, Geosynthetic Reinforced Soil–Integrated Bridge Systems (GRS-IBS), reinforced embankments, and landfill containment systems [14]. As shown in **Table 1**, geosynthetics such as geogrids, geotextiles, and geocomposites have been effective across various structures, environments, functions, and backfill materials [16] [17] [18] [19] [20] [21]. These successes support the potential of geosynthetic solutions for Martian soil applications.

Table 1. Examples of terrestrial geosynthetic-reinforced soil structures.

Structure	Function	Location	Height (m)	Geosynthetic Material	Backfill Soil
Mechanically Stabilized Earth (MSE) Wall [16]	Supports heavy equipment on mine pad.	Nevada, USA Cortez Hills Mine	29	PET Uniaxial geogrids	Predominantly well-graded gravels and cobbles.
Reinforced Soil Slope (RSS) [16]	Highway embankment on valley slope.	West Virginia, USA Route 10 Highway	36.6	PET Uniaxial geogrids	Crushed bedrock composed of sandstone, shale, siltstone, and coal.
Geosynthetic Reinforced Soil-Integrated Bridge System (GRS-IBS) [17]	Supports bridge beams directly with backfill.	Defiance County, Ohio, USA	5	PP Woven Geotextile	AASHTO No.89 stone.
Riverbank Retaining Wall [18]	Stabilizes riverbank and protects against seismic activity.	Christchurch, New Zealand	3.4	HDPE Geogrid	Pit-run granular material.
Runway Embankment [19]	Supports runway construction in steep Himalayan terrain.	Sikkim, India	74	PET Geogrid + Steel Mesh	Mixture of soil and rock.
Landfill Expansion Berm [20]	Enables vertical landfill expansion with containment stability.	Guangzhou, China	37	PET Woven Geotextile	Municipal solid waste.
GRS Approach Embankment [21]	Stabilizes the bridge approach embankments.	Dakar, Senegal	5.2	PP Geocomposite	Dune sands.

Selected examples of presently existing geosynthetic-reinforced soil structures on Earth, illustrating various applications, materials, heights, and functions. Note: This is not a comprehensive list of all uses of geosynthetic structures.

These terrestrial applications demonstrate that geosynthetically reinforced soil structures can offer high strength and adaptability under a range of conditions. However, their performance in Martian soils remains untested, requiring targeted studies using geotechnical simulants.

Numerous studies have examined how reinforcement configuration, loading, and environment influence the bearing capacity of reinforced soils on Earth. Other than full scale field tests, physical model tests have emerged as the most reliable of methods to investigate deformation and load-bearing behavior in controlled conditions [22], [23], [24], [25], [26], [27], [28], [29], [30], [31]. For example, Verma and Mittal (2023) showed using physical model tests that had secondary reinforcement beneath the footing significantly improved stability, reducing both settlement and face displacement [22]. Wang et al. (2024) and Xu et al. (2023), using similar methods, found that vertical and lateral deformations scale linearly with load and are sensitive to setback distance, with larger setbacks reducing displacement [23], [29]. Zheng et al. (2019a, 2019b) demonstrated that reinforcement spacing strongly influences vertical settlement under both static and dynamic conditions, with tighter spacing limiting deformation [27], [28]. These findings from Earth-based studies guide the approach for Mars.

This study aims to pioneer an experimental methodology for evaluating geosynthetic reinforcement under Martian soil conditions and to develop a complementary theoretical framework for predicting performance. The work uses a novel load-bearing test setup for geogrid-reinforced Martian soil, adapted from geosynthetic reinforced soil (GRS) bridge abutment model tests. In this setup, the retaining wall is a prefabricated acrylic board with a flange which was not structurally connected to the geogrid layers, producing a failure mechanism distinct from conventional reinforced soil structures. Using this configuration, the study examines how reinforcement spacing and material stiffness influence performance in a custom-prepared Martian soil simulant. While the findings provide insight into optimal reinforcement configurations within the tested conditions, the broader aim is to establish a replicable, resource-efficient framework for assessing new soil simulants and novel geosynthetic materials. In doing so, this work provides both an experimental and an analytical basis for subsequent investigations into load-bearing infrastructure on Mars.

II. Experimental Methodology

2.1 Martian Soil Simulant

Replicating Martian soil for geotechnical testing requires approximating key mechanical properties. Grain size distribution is the primary consideration, as it governs shear strength, compaction behavior, and deformation response [32], [33], [34], [35], [36]. Studies on Martian soil analogs have shown that matching the particle size distribution alone can be sufficient to simulate load bearing and deformation behavior, even without duplicating the exact mineral or chemical composition [35], [36].

This study adopts the grain size profile of bright eroded mantles (BEM) at Oxia Planum, the selected landing site of the ExoMars rover. Grain size data for BEM were taken from values reported by Slyuta et al. (2024) [10]. BEM was chosen because it represents one of the finest-grained surface materials at the site, markedly different from the coarse, well-graded granular backfills typically used in terrestrial reinforced soil construction. Evaluating geogrid reinforcement in such a fine-grained context allows us to test performance under conditions not commonly encountered in Earth-based designs. The particle size distributions of the target BEM reference and the model backfill mixture are shown in **Fig. 1.** In consideration of cost and material availability, the model backfill was formulated as a 1:1 ratio of quartz sand and fly ash, adapted from the VI-M1 Martian soil simulant recipe developed by Slyuta et al. (2024) [10]. The particle-size distributions of the BEM reference and the sand–fly ash backfill closely coincide (**Fig. 1**). A total of 50 kg of quartz sand and 50 kg of fly ash were mixed to create the backfill. The sand component contained approximately 30% of particles in the 10–1.0 mm range, 30% in the 1.0–0.5 mm range, and 40% in the 0.5–0.25 mm range. The fly ash component contained about 50% of particles in the 0.25–0.1 mm range, 20% in the 0.1–0.005 mm range, 15% in the 0.005–0.001 mm range, and 15% finer than 0.001 mm.

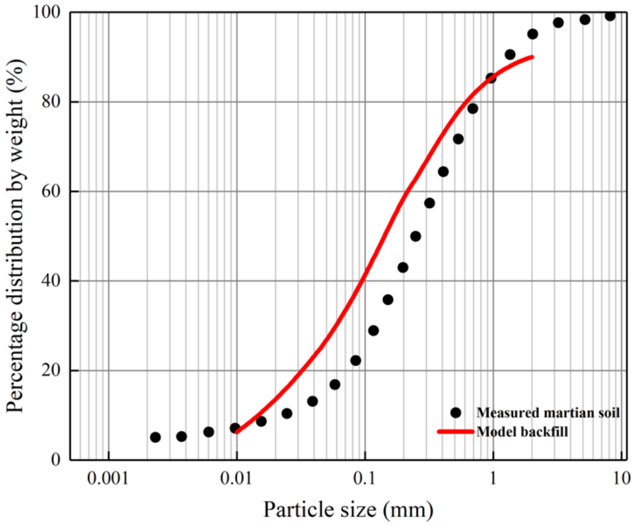

Fig. 1. Cumulative particle size distribution of the target BEM simulant and the model backfill.

2.2 Reinforcement Material

Three types of geogrid reinforcement were used in the experiments (glass-fibre, metal, and acrylic), each providing a different tensile or flexural stiffness to the system. Each reinforcement layer spanned the full width of the model, extending from the back of the facing wall to the rear wall of the container (**Fig. 3c**). Unlike typical FHWA procedures in which reinforcement layers are secured tautly to the wall facing [37], in this study the geogrid layers were not attached or tensioned at the facing. Instead, each layer was laid loosely on top of its respective backfill lift, with its front edge simply placed against the wall facing. This deviation from standard practice is noteworthy and likely contributed to the distinct failure mechanism described later.

2.3 Experimental Setup and Procedure

This experiment employs a novel and accessible load-bearing test setup for geosynthetic-reinforced Martian soil, adapted from methodologies used in geosynthetic reinforced soil (GRS) bridge abutment model tests. (**Fig. 2**). Using a procedure inspired by bridge abutment model tests offers several advantages for evaluating

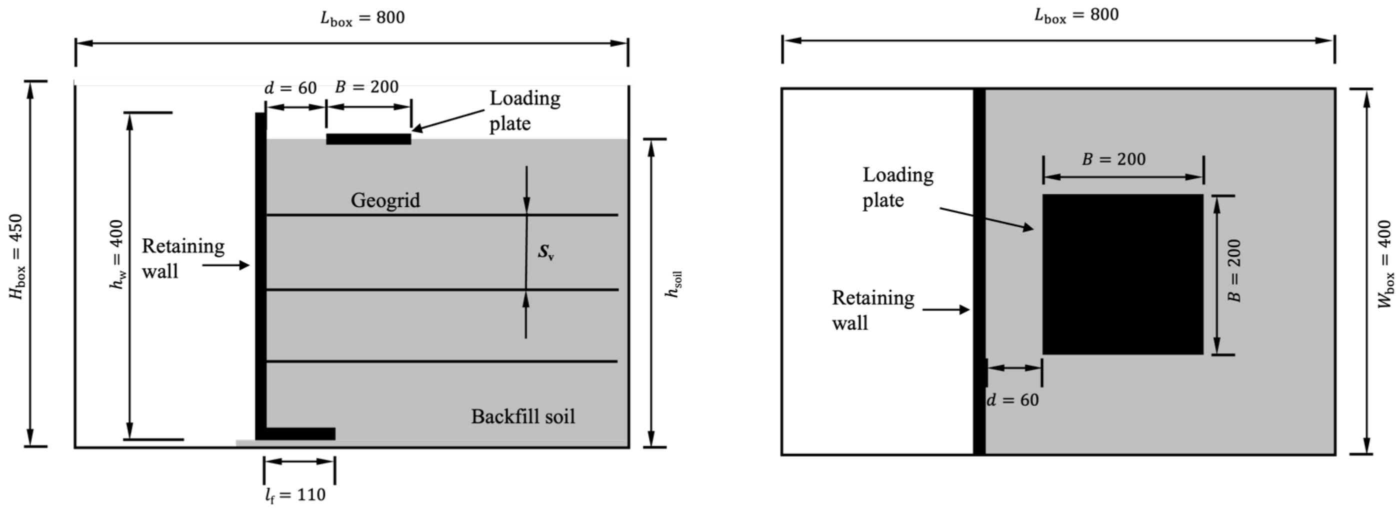

(a) (b)

Fig. 2. Experimental setup: (a) side view; (b) top view.

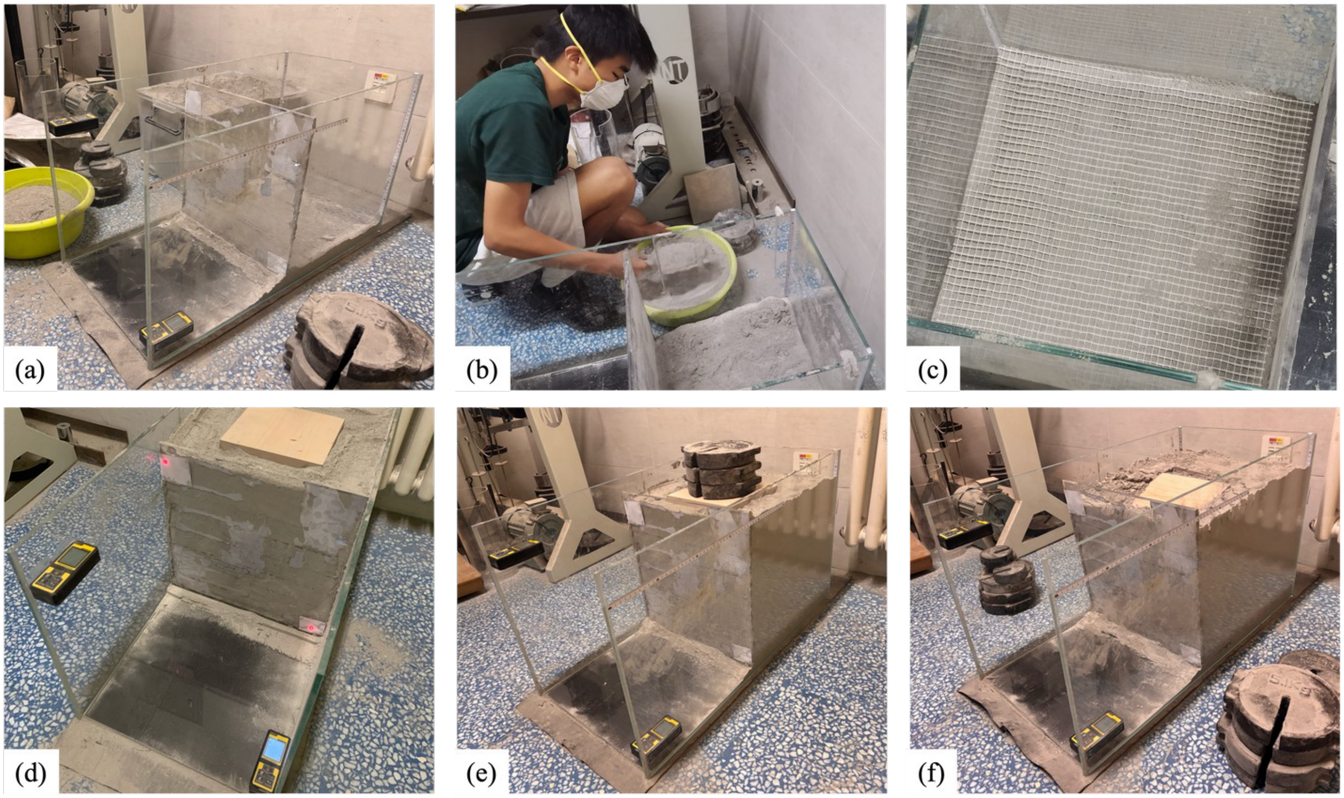

Fig. 3. Experimental procedure: (a) unfilled experimental container with retaining wall placed on a 10 mm base layer; (b) manual filling of backfill; (c) glass fibre geogrid placed on a backfill lift; (d) fully filled backfill at zero applied load, with laser displacement sensors positioned to measure facing movement; (e) fully filled backfill at 150 N load applied by calibrated weights (f) post-failure setup with weights removed, failure patterns and settlement visible.

the load-bearing capacity of a new and previously untested backfill. The model allows bearing capacity to be quantitatively assessed from displacement data, and failure mechanisms to be observed qualitatively through the transparent side walls (**Fig. 3f**).

The model setup was constructed in a rigid transparent glass container with internal dimensions $L_{box} = 800$ mm, $W_{box} = 400$ mm, and $H_{box} = 450$ mm (**Fig. 2**). The container walls provide lateral confinement to approximate plane-strain conditions under load. These dimensions were chosen to allow controlled layering of backfill and reinforcement, straightforward installation of displacement sensors, and clear visual access to the soil mass during loading. While a larger model would improve stress similarity to field conditions [29], the chosen dimensions permit manual backfill placement, limit the amount of simulant required, and remain sufficient for accurate measurements—qualities essential for efficiently testing new backfill material.

The backfill height was set to $h_{soil} = 400$ mm. The retaining structure was an L-shaped acrylic wall with a vertical height $h_w = 400$ mm, base flange length $l_f = 120$ mm, and thickness $t = 10$ mm, which stood on top of a 10 mm base layer of backfill to minimize wall-container contact. Acrylic was selected for its high flexural rigidity at this scale, which minimizes deformation and reduces experimental variability. The wall was placed at a distance 400 mm from the rear boundary of the container at the start of each test.

The loading plate was a square wooden plate with side length $B = 200$ mm, which was positioned on the soil surface with a setback of $d = 60$ mm from the vertical wall to ensure representative soil–wall deformation behavior. Two laser displacement sensors were mounted at the top-left and bottom-right corners of the wall to measure facing displacement throughout each test (**Fig. 3d**).

Before each trial, a 10 mm base layer of backfill was placed beneath the facing wall. Backfill was manually placed and leveled with minimal mechanical compaction (**Fig. 3b**). This approach reflected anticipated Martian construction conditions, where compaction may be limited by environmental and operational constraints. For tests including reinforcement, geogrid layers were placed after leveling a backfill lift to the designated elevation. Layer heights were determined using two tape measures fixed to the back corners of the container (±1 mm).

Once the backfill placement was complete, the loading plate was set in position, and baseline displacement readings were taken from both sensors. Loading was applied in increments of 1.275 kg by placing calibrated weights directly onto the plate (**Fig. 3e**). After each increment, displacement at both sensor locations was recorded. The tests were terminated when failure of the structure occurs (**Fig. 3f**). Failure was defined as wall displacement exceeding 5% of the fill height (20 mm) relative to the unloaded position. Failure was also recorded if a collapse occurs that prevented further measurements, or if the top lift shifted enough for the weights on the loading plate to tip forward and fall. For each trial, the entire model was reconstructed to minimize cross-test variability caused by unaccounted for compaction.

2.4 Experimental Conditions

After a series of preliminary tests to determine the most efficient experimental setup and procedure, 7 tests were conducted to examine the effects of vertical displacement and reinforcement material on bearing capacity. To isolate spacing effects from material variability, a series of tests were conducted using only the glass-fibre geogrid. To isolate reinforcement material from vertical spacing, two additional tests were performed using a single layer of a metal geogrid and an acrylic grid placed at mid-height. The complete program is summarized in **Table 2**.

Table 2. All test configurations of the experimental program.

Test No.	Reinforcement Material	Number of Layers
1	None (Control)	0
2	Glass-fibre geogrid	1
3	Glass-fibre geogrid	2
4	Glass-fibre geogrid	3
5	Glass-fibre geogrid	4
6	Metal geogrid	1
7	Acrylic geogrid	1

III. Experimental Results

This section consists of four parts: first, observed failure mode; second, effect of geogrid vertical spacing on load–displacement response and bearing capacity; third, effect of reinforcement material stiffness; and fourth, an analytical model calibrated to the data.

3.1 Failure mode

Under vertical loading, the reinforced soil body consistently exhibited a sliding failure mode. A pronounced example from a preliminary test is shown in **Fig. 4** In the primary test series, the same failure mechanism occurred, though the tests were typically stopped once the

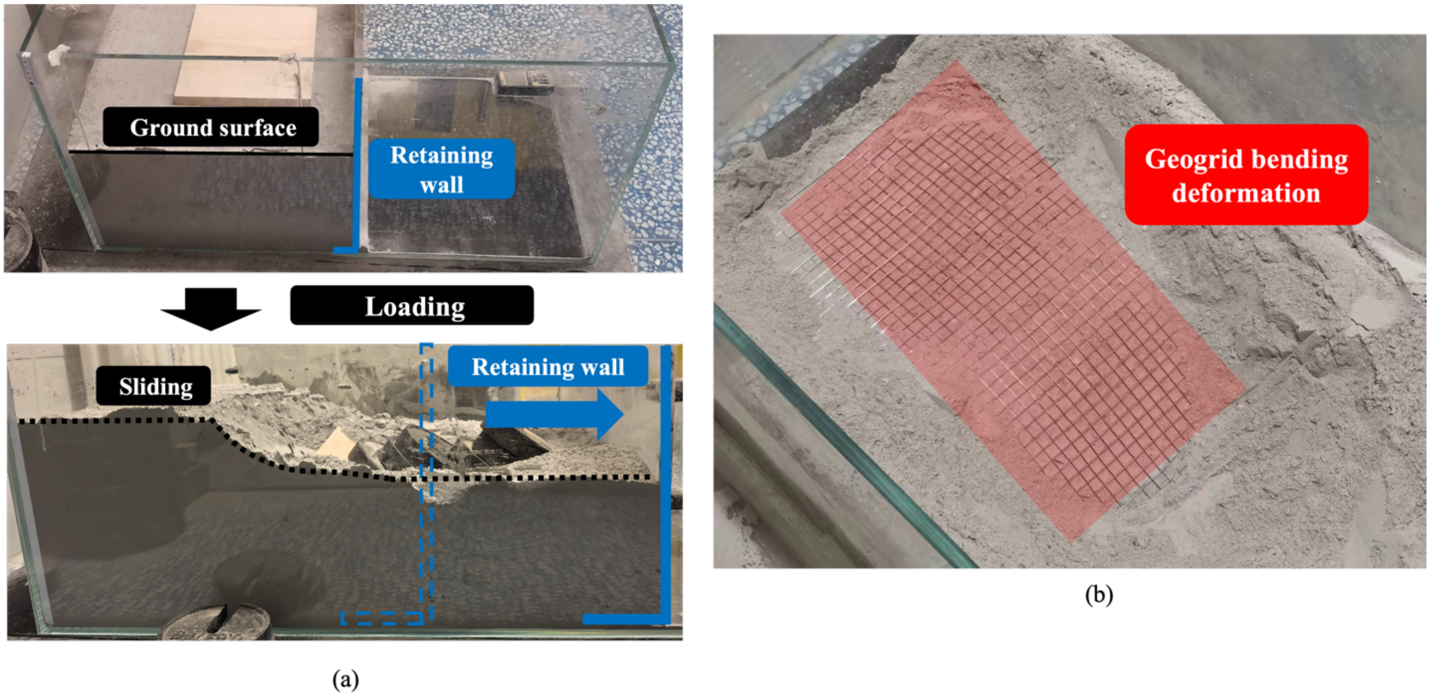

(a)

(b)

Fig. 4. Failure modes from preliminary testing: (a) wall sliding; (b) geogrid bending deformation.

displacement reached the 5% threshold, so the outward sliding was less dramatic (e.g. **Fig. 3f**).

During all tests, none of the geogrid reinforcement ruptured. Instead, the geogrids were bent down towards the retaining wall. A pronounced example of this bending motion is shown in **Fig. 4b** by a metal geogrid (highlighted in red). Each geogrid continued to tie together the moving soil wedge and the stable soil mass behind the failure plane, bending as the wedge slid outward. This behavior suggests that the reinforcement was primarily engaged in bending instead of tension.

3.2 Effect of reinforcement spacing

A series of tests was conducted using only the glass-fibre geogrid to isolate spacing effects from material variability.

The total height of the backfill is constant while the vertical spacing of the geogrids was tested at 200, 133, 100 mm, and 80 mm corresponding to 1, 2, 3, and 4 layers of geogrid respectively. Notably, at 0 layers of the geogrid (control), the structure collapsed before it was filled. Additionally, at 4 layers of the glass-fibre geogrid, the maximum testing capacity of the experimental setup was reached (600N), as the addition of weights would be a safety hazard.

Fig. 5a shows load–displacement datapoints in increments of 12.495 N. As the reinforcement spacing is reduced, the load–displacement response becomes stiffer. As shown in **Fig. 5(b)**, closely spaced layers (100 mm) sustained nearly 8 times the load of the model with the largest spacing (200 mm).

3.3 Effect of reinforcement material

Fig. 6a shows load–displacement curves for single-layer geogrid reinforcements placed at mid-height, spanning flexural stiffness values of ~32, 614, and 3200 N·mm² for glass-fibre, steel, and acrylic grids respectively. Flexural stiffness was used instead of tensile strength because no reinforcement ruptured during testing: all geogrids exhibited downward bending toward the retaining wall, indicating that bending resistance, not tensile capacity, governed performance for this model.

As shown in **Fig. 6b**, bearing capacity increased with stiffness, from ~80 N for glass-fibre to ~120 N for steel and ~180 N for acrylic, though gains diminished at the highest stiffness.

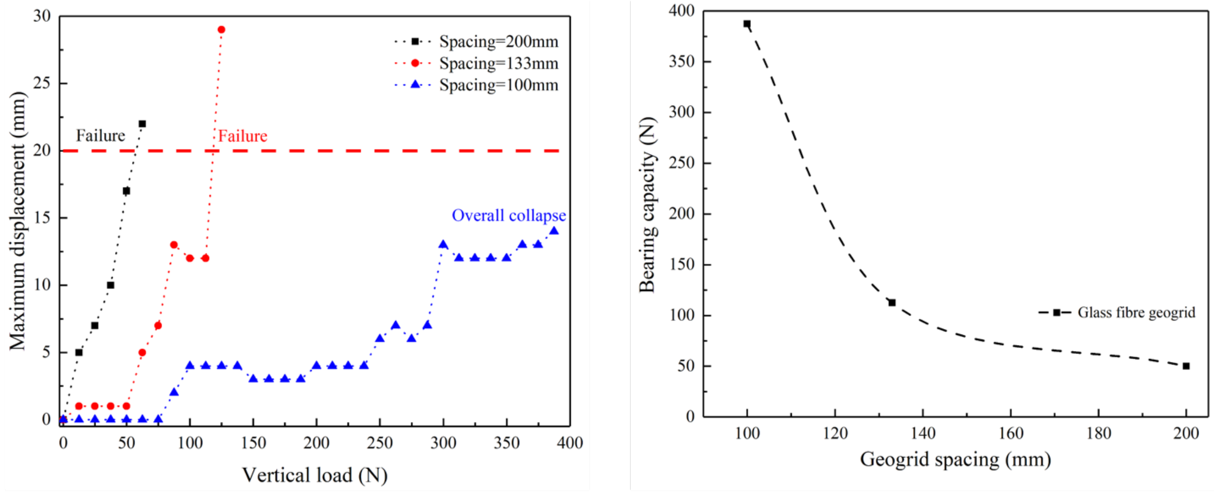

(a)

(b)

Fig. 5. Effect of geogrid spacing on bearing capacity: (a) maximum displacement point of facing wall (dashed red line represents failure threshold); (b) bearing capacity under different geogrid spacings.

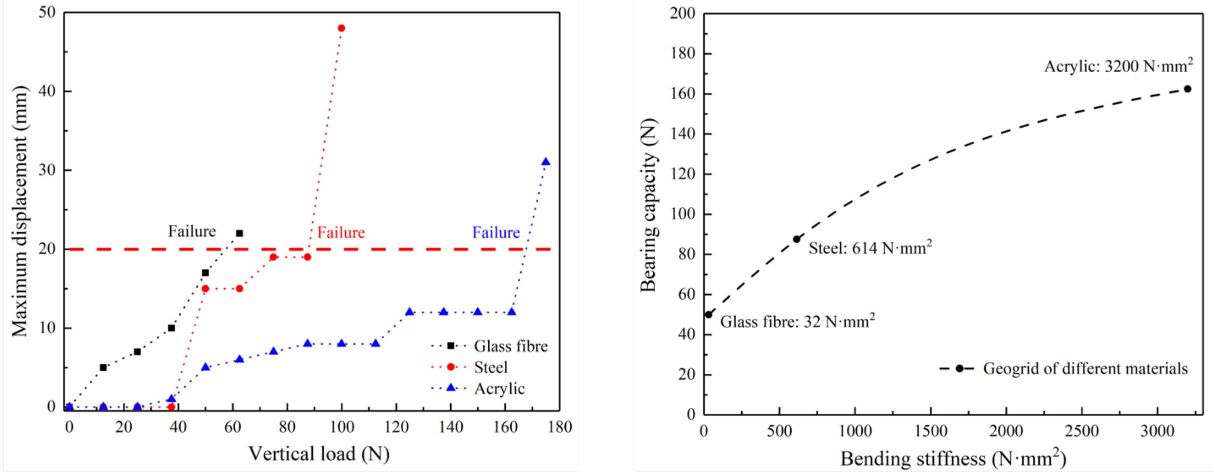

(a)

(b)

Fig. 6. Effect of geogrid material on bearing capacity: (a) maximum displacement point of facing wall (dashed line represents failure threshold); (b) bearing capacity under different reinforcement material bending stiffness.

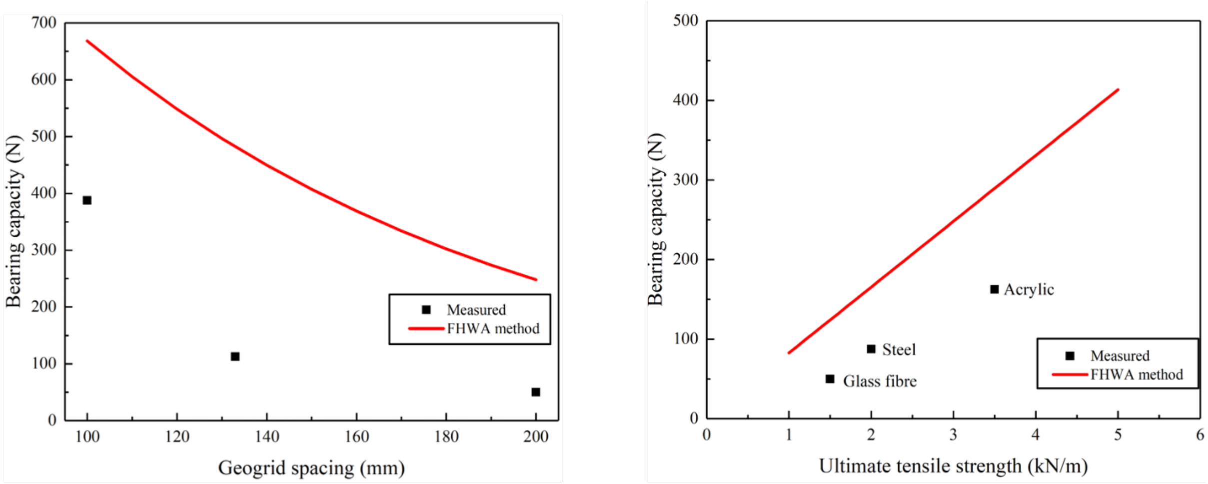

(a) (b)

Fig. 7. Comparison between FHWA-predicted and measured bearing capacity: (a) effect of geogrid spacing; (b) effect of geogrid tensile strength.

3.4 Theoretical Analysis

3.4.1 Comparison with FHWA method

The Federal Highway Administration (FHWA) provides a semi-empirical formula for the ultimate bearing capacity of a geosynthetic-reinforced soil abutment. It assumes that the backfill soil is in a passive state, indicating that the wall is pushing the soil all the time until abutment failure. It also assumes that the failure of geosynthetic reinforced soil under maximum vertical load occurs when the stress in the reinforcement geogrids exceeds their ultimate tensile strength. Thus, the FHWA bearing capacity is expressed as Eq. 1, with the passive earth pressure coefficient defined by Eq. 2.

$$\mathrm{p_u} = \left[0.7^{\frac{\mathrm{s_v}}{6\mathrm{d_{max}}}} \cdot \frac{\mathrm{T_f}}{\mathrm{s_v}}\right]\mathrm{K_p} \tag{1}$$

$$K_p = \tan^2\left(45^\circ + \frac{\varphi}{2}\right) \tag{2}$$

To compare the FHWA prediction with our model test results, parameters for Eqs. 1 and 2 were chosen to match the experimental conditions. The maximum particle size $\mathrm{d_{max}}$ was 6mm (**Fig. 1**). The internal friction angle of the soil φ was 30 degrees. The ultimate tensile strengths of the three geogrids, $T_{f(glass)}$, $T_{f(steel)}$, and $T_{f(acrylic)}$ were taken as 1.5 kN/m, 2.0 kN/m, and 3.5 kN/m, respectively.

As shown in **Fig. 7**, the FHWA method significantly overestimates the ultimate bearing capacity of the model, irrespective of geogrid material type or spacing, with some predictions exceeding the actual values by multiples of 3 to 4.

This significant discrepancy can be largely contributed to the failure modes of the geosynthetic reinforced soil. The FHWA method, specifically Eq. 1, assumes that the failure of the abutment is caused by the tensile failure of the geogrids. However, in this experiment the precast retaining wall was not attached to the geogrids, resulting in a sliding primary failure mode. This is also the reason why none of the geogrids ruptured throughout all the tests. It was observed that the geogrids instead performed bending deformation to transfer and diffuse the additional stress from vertical loads and the self-weight stress from the backfill soil (**Fig. 4b**). Thus, it is more appropriate to characterize the material's influence on the ultimate bearing capacity of geosynthetic reinforced soil using its resistance to bending deformation—bending stiffness E— where E is the elastic modulus of the material, and I is the moment of inertia of the cross-section.

Therefore, to predict the ultimate bearing capacity of this specific wall–reinforcement system, a new theoretical model is needed that accounts for the sliding failure mechanism and the bending dominated action of the geogrids.

3.4.2 New Theoretical model for bearing capacity

Based on the observed failure mechanism, a force equilibrium analysis of the retaining wall was developed (see **Fig. 8** for the diagram).

There are two significant horizontal forces acting upon the reinforcement: the active earth pressure p_a provided by the backfill soil and the additional horizontal load p' caused by the vertical load p. The resistance to sliding is primarily provided by the frictional force between the wall base plate and the foundation soil, which depends on the self-weight of the soil G_{soil} above the wall foundation and the vertical load p'' which comes from p transmitting to the base plate. Neglecting any geogrid contribution, force equilibrium yields the equations 3 – 8:

$$p_a W + p'(H-d)(B+2d\tan\theta) = \mu\left(G_{soil} + p'' l_f W\right) \tag{3}$$

$$p_a = \frac{1}{2}\gamma K_a H^2 \tag{4}$$

$$K_a = \tan^2\left(45^\circ - \frac{\varphi}{2}\right) \tag{5}$$

$$p' = \frac{B^2}{(B+2d\tan\theta)^2}p \tag{6}$$

$$G_{soil} = \gamma H l_f W \tag{7}$$

$$p'' = \frac{B^2}{W L_{soil}}p \tag{8}$$

These equations include the Rankine active earth pressure coefficient K_a, the maximum base-wall friction coefficient μ between the wall footing and foundation soil, the unit weight of the soil γ, the internal friction angle φ, and the diffusion angle θ (see **Fig. 8** for a depiction of these parameters).

When added, the geogrids redistribute a portion of the vertical force. While the total load remains unchanged, the horizontal earth pressure

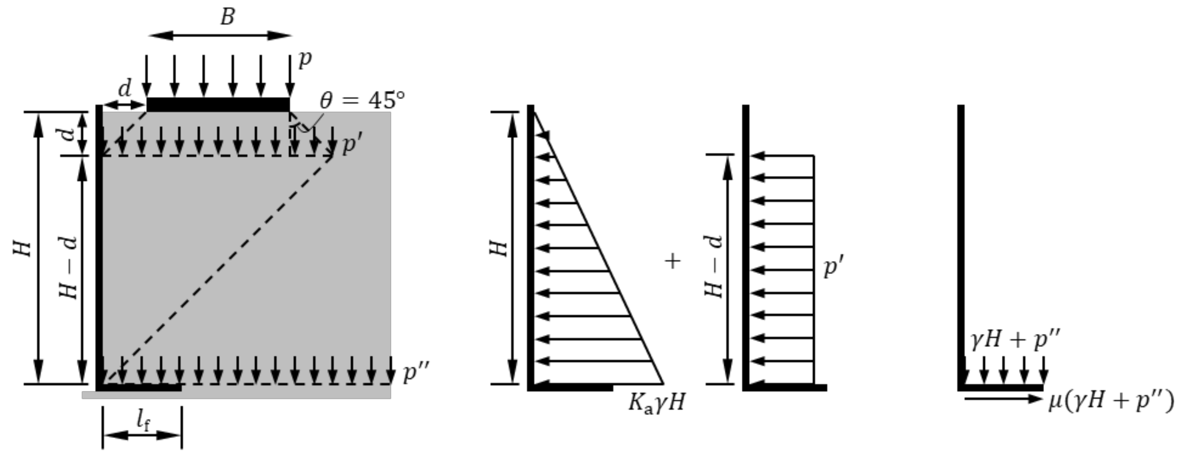

Fig. 8. Force distribution on the retaining wall: center, active earth pressure and pressure by additional load; right, friction caused by pressure on flange.

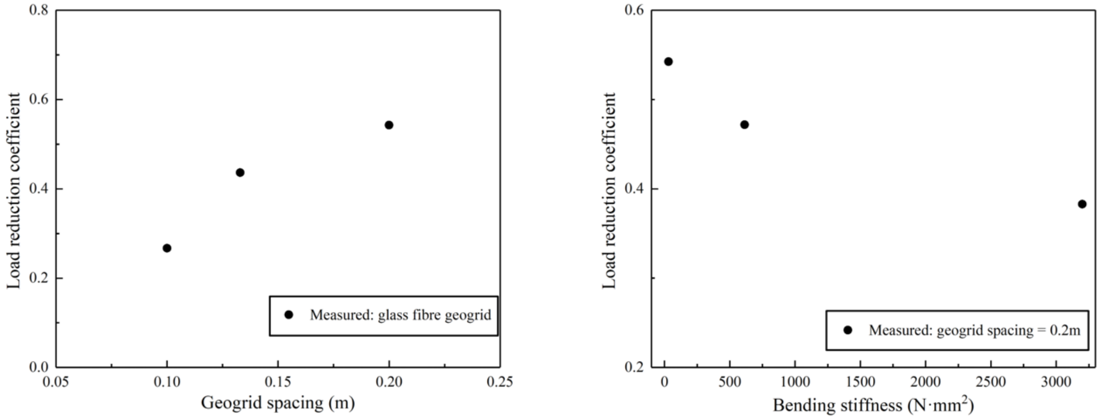

(a) (b)

Fig. 9. Load reduction factor: (a) by reinforcement spacing; (b) by reinforcement stiffness.

on the wall is reduced. Thus, a load reduction factor ε is introduced to quantify the reduction in lateral pressure due to the reinforcement. The equilibrium condition for the reinforced system can be written as Eq. 9, and by rearrangement we can derive an expression for ε, which is shown in Eq. 10, where P_{ult} (kN/m^2) is the ultimate vertical load of geosynthetically reinforced soil.

$$\varepsilon[p_a W + p'(H-d)(B + 2d\tan\theta)] \\ = \mu\left(G_{soil} + p'' l_f W\right) \tag{9}$$

$$\varepsilon = \frac{\mu\left(\gamma l_f H W + \frac{B^2 l_f W}{W L_{soil}} p_{ult}\right)}{\frac{1}{2}\gamma H^2 W \tan^2\left(45° - \frac{\varphi}{2}\right) + \frac{B^2(H-d)}{B+2d\tan\theta} P_{ult}} \tag{10}$$

All variables in Eq. 10 except P_{ult} are known constants from the experiment. Therefore, the load reduction coefficient ε can be calculated accordingly under specific geogrid materials and vertical spacing conditions. Among these, $\mu = 0.4$, $\gamma = 15.5 kN/m^3$, $\theta = 45°$, $\varphi = 30°$, other parameters are taken according to dimensions specified in the methodology. The value of the load reduction factor ε of each measured trial is shown in **Fig. 9.**

As shown in **Fig. 9**, the load reduction coefficient decreases with smaller geogrid spacing and greater bending stiffness as closer spacing reduces the horizontal earth pressure on the wall, while higher bending stiffness enables the geogrid to distribute loads over a larger soil volume.

Therefore, it can be considered that the load reduction coefficient ε is a function of the geogrid spacing s_v and geogrid flexural rigidity EI. Thus, a multiple linear regression yielded the following relation (Eq. 11), where $R^2 = 0.92$.

$$\varepsilon(s_v, EI) = 2.651 s_v - 5.398 \times 10^{-5} EI + 0.018 \tag{11}$$

Substituting this fitted relationship for ε back into the equilibrium condition (Eq. 10), the explicit expression for the ultimate bearing capacity of the reinforced soil system, $p_{ult}(s_v, EI)$, was derived (Eq. 12).

$$p_{ult} = \frac{\frac{1}{2}\gamma H^2 W \varepsilon(s_v, EI)\tan^2\left(45° - \frac{\varphi}{2}\right) - \mu\gamma l_f H W}{\frac{\mu B^2 l_f W}{W L_{soil}} - \frac{\varepsilon(s_v, EI) B^2 (H-d)}{B + 2d\tan\theta}} \tag{12}$$

This equation is tailored to the sliding and bending failure mechanism observed in our experiments. Its accuracy decreases as geogrid spacing and bending stiffness deviate from the tested ranges, since ε was obtained through multiple linear regression, which does not capture nonlinear effects such as concavity. However, with more data points, this can be used to estimate the loading capacity for drastically different geogrid layouts and materials, and the general theoretical analysis strategy can be further adapted to fit other unique circumstances.

IV. Conclusions

This paper presented experimental results from physical model tests on geosynthetic reinforced soil (GRS) made with custom made Martian bright eroded mantels (BEM) simulant. These results were used to evaluate and optimize geogrid reinforcement to improve the bearing capacity of simulated Martian soils, which is crucial towards future Martian habitation. The model test setup was adapted from geosynthetic reinforced soil (GRS) bridge abutment experiments. Notably it consisted of a prefabricated retaining wall facing that was not structurally connected to the geogrid layers. Seven tests were conducted in total with geogrid spacing and geogrid material being varied independently. Based on the findings, the following conclusions were drawn:

- Due to the unique setup and soil, models exhibit a sliding failure mechanism rather than the conventional tensile rupture of reinforcement. Under vertical loading, the retaining wall and backfill displaced outward as a composite wedge, while the geogrid layers bent downward along the failure plane without tearing. This shows that the reinforcement primarily acted through bending to interlock the moving soil wedge with the stable backfill, redistributing stresses and delaying collapse. Thus, flexural resistance, rather than tensile strength, governed the ultimate bearing capacity in this configuration.
- Close vertical spacing of geogrid layers improves the load-bearing performance of models. Reducing the distance between reinforcement layers produces a stiffer load–displacement response and enables a substantially higher supported load compared to widely spaced or unreinforced soil.
- Increased stiffness of the geosynthetic reinforcement improves the load-bearing performance of models. Geogrid layers with higher bending rigidity provided greater bearing capacity, indicating improved load transfer within the reinforced soil mass. However, performance gains diminished at the highest stiffness tested, thus, an optimal range of reinforcement stiffness exists, beyond which additional rigidity yields limited benefit.
- The newly proposed analytical method for estimating ultimate bearing capacity accounts for the bending-dominated reinforcement mechanism observed in the tests, which offers a more accurate framework than conventional tension-based models for this setup. Thus, such approaches are necessary for reliable design of geosynthetic reinforced soil structures, especially those that deviate from common terrestrial structures.

References

[1] J. Farrier, “On martian soil,” *Civ. Eng.*, vol. 70, no. 4, pp. 46-47, Apr. 2000.

[2] R. Hedayati and V. Stulova, “3D Printing of Habitats on Mars: Effects of Low Temperature and Pressure,” *Materials*, vol. 16, no. 14, Jan. 2023, doi: 10.3390/ma16145175.

[3] D. M. Hassler *et al.*, “Mars’ Surface Radiation Environment Measured with the Mars Science Laboratory’s Curiosity Rover,” *Science*, vol. 343, no. 6169, p. 1244797, Jan. 2014, doi: 10.1126/science.1244797.

[4] N. Barlow, *Mars: an Introduction to Its Interior, Surface and Atmosphere*. Cambridge, UNITED KINGDOM: Cambridge University Press, 2008.

[5] F. He *et al.*, “Martian Dust Storms: Reviews and Perspective for the Tianwen-3 Mars Sample Return Mission,” *Remote Sens.*, vol. 16, no. 14, Art. no. 14, Jan. 2024, doi: 10.3390/rs16142613.

[6] R. Team, “Characterization of the Martian Surface Deposits by the Mars Pathfinder Rover, Sojourner,” *Science*, vol. 278, no. 5344, pp. 1765–1768, Dec. 1997, doi: 10.1126/science.278.5344.1765.

[7] R. D. Lorenz *et al.*, “Lander and rover histories of dust accumulation on and removal from solar arrays on Mars,” *Planet. Space Sci.*, vol. 207, p. 105337, Nov. 2021, doi: 10.1016/j.pss.2021.105337.

[8] G. A. Landis and P. P. Jenkins, “Measurement of the settling rate of atmospheric dust on Mars by the MAE instrument on Mars Pathfinder,” *J. Geophys. Res. Planets*, vol. 105, no. E1, pp. 1855–1857, 2000, doi: 10.1029/1999JE001029.

[9] D. Crisp, A. Pathare, and R. C. Ewell, “The performance of gallium arsenide/germanium solar cells at the Martian surface,” *Acta Astronaut.*, vol. 54, no. 2, pp. 83–101, Jan. 2004, doi: 10.1016/S0094-5765(02)00287-4.

[10] E. N. Slyuta *et al.*, “Martian soil-analogue VI-M1 for large-scale geotechnical experiments,” *Planet. Space Sci.*, vol. 251, p. 105959, Oct. 2024, doi: 10.1016/j.pss.2024.105959.

[11] B. J. Chow, T. Chen, Y. Zhong, and Y. Qiao, “Direct Formation of Structural Components Using a Martian Soil Simulant,” *Sci. Rep.*, vol. 7, no. 1, p. 1151, Apr. 2017, doi: 10.1038/s41598-017-01157-w.

[12] O. K. Soureshjani and A. Massumi, “Martian buildings: structural forms using in-place sources,” *Sci. Rep.*, vol. 12, no. 1, p. 21992, Dec. 2022, doi: 10.1038/s41598-022-25507-5.

[13] J. Liu *et al.*, “In-situ resources for infrastructure construction on Mars: A review,” *Int. J. Transp. Sci. Technol.*, vol. 11, no. 1, pp. 1–16, Mar. 2022, doi: 10.1016/j.ijtst.2021.02.001.

[14] W. W. Müller and F. Saathoff, “Geosynthetics in geoenvironmental engineering,” *Sci. Technol. Adv. Mater.*, vol. 16, no. 3, p. 034605, June 2015, doi: 10.1088/1468-6996/16/3/034605.

[15] S. M. Hejazi, M. Sheikhzadeh, S. M. Abtahi, and A. Zadhoush, “A simple review of soil reinforcement by using natural and synthetic fibers,” *Constr. Build. Mater.*, vol. 30, pp. 100–116, May 2012, doi: 10.1016/j.conbuildmat.2011.11.045.

[16] S. Mandavkar and M. Weldu, “Geogrid reinforced soil structures reach new heights - Geosynthetics Magazine,” Geosynthetics Magazine. [Online]. Available: https://geosyntheticsmagazine.com/2019/06/01/geogrid-reinforced-soil-structures-reach-new-heights/ (accessed July. 15, 2025).

[17] M. Adams, J. Nicks, T. Stabile, W. Schlatter, and J. Hartmann, “Geosynthetic reinforced soil integrated bridge system interim implementation guide,” Federal Highway Administration (US), 2012.

[18] M. Dobie, G. R. Stevens, and S. J. Collin, “Performance of a reinforced soil retaining wall during the Christchurch earthquakes,” *11th Australia New Zealand Conference on Geomechanics (ANZ 2012)*, Jul. 2012.

[19] Maccaferri, “Construction of New Airport at Pakyong, Sikkim, India,” Maccaferri, India, Case History CH/INT/SR007-IN, Rev 01, Oct. 2012. [Online]. Available: https://www.issmge.org/filemanager/article/16/Maccaferri-New_Airport_Sikkim.pdf (accessed July. 11, 2025)

[20] H. Ke, P. Ma, J. Lan, Y. Chen, and H. He, “Field behaviors of a geogrid reinforced MSW slope in a high-food-waste-content MSW landfill: A case study,” *Geotext. Geomembr.*, vol. 49, no. 2, pp. 430–441, Apr. 2021, doi: 10.1016/j.geotexmem.2020.10.017.

[21] J.-B. Duquet, P. Garcin, and A. Nancey, “The use of a geosynthetic-reinforced wall in the construction of bridge-access embankments in Dakar (Senegal),” presented at GeoAfrica 2009, Cape Town, South Africa, Sept. 2009.

[22] A. Verma and S. Mittal, “Comparative assessment of stability of GRS abutments through 1 g physical model tests for field implementation,” *Transp. Geotech.*, vol. 42, p. 101056, Sept. 2023, doi: 10.1016/j.trgeo.2023.101056.

[23] Q. Wang, C. Xu, P. Shen, G. Li, and C. Zhao, “Experimental and theoretical studies on deformation characteristics of Geosynthetic-Reinforced Soil (GRS) abutments induced by vertical loads,” *Geotext. Geomembr.*, vol. 52, no. 5, pp. 925–940, Oct. 2024, doi: 10.1016/j.geotexmem.2024.05.008.

[24] C. Xiao, J. Han, and Z. Zhang, “Experimental study on performance of geosynthetic-reinforced soil model walls on rigid foundations subjected to static footing loading,” *Geotext. Geomembr.*, vol. 44, no. 1, pp. 81–94, Feb. 2016, doi: 10.1016/j.geotexmem.2015.06.001.

[25] J. Deng, J. Zhang, Z. Qi, Y. Zheng, and J. Zheng, “Experimental study on the load bearing behavior of geosynthetic reinforced soil bridge abutments on yielding foundation,” *Geotext. Geomembr.*, vol. 51, no. 5, pp. 165–178, Oct. 2023, doi: 10.1016/j.geotexmem.2023.06.003.

[26] Y. Jia, J. Zhang, and Y. Zheng, “Model Test of the Influence of Cyclic Traffic Load on the Cumulative Deformations of GRS Bridge Abutment,” in *Proceedings of the 5th International Conference on Transportation Geotechnics (ICTG) 2024, Volume 8*, vol. 409, C. Rujikiatkamjorn, J. Xue, and B. Indraratna, Eds., in Lecture Notes in Civil Engineering, vol. 409. , Singapore: Springer Nature Singapore, 2025, pp. 57–67. doi: 10.1007/978-981-97-8241-3_7.

[27] Y. Zheng, P. J. Fox, P. B. Shing, and J. S. McCartney, “Physical Model Tests of Half-Scale Geosynthetic Reinforced Soil Bridge Abutments. I: Static Loading,” *Journal of Geotechnical and Geoenvironmental Engineering*, vol. 145, no. 11, Nov. 2019, doi: 10.1061/(asce)gt.1943-5606.0002152.

[28] Y. Zheng, J. S. McCartney, P. B. Shing, and P. J. Fox, “Physical Model Tests of Half-Scale Geosynthetic Reinforced Soil Bridge Abutments. II: Dynamic Loading,” *Journal of Geotechnical and Geoenvironmental Engineering*, vol. 145, no. 11, Aug. 2019, doi: 10.1061/(asce)gt.1943-5606.0002158.

[29] C. Xu *et al.*, “Scaled Model Tests Investigating Deformation Characteristics of Geosynthetic Reinforced Soil (GRS) Abutments under Vertical Loads,” *Materials*, vol. 16, no. 13, p. 4601, June 2023, doi: 10.3390/ma16134601.

[30] X. Cai, S. Li, H. Xu, L. Jing, X. Huang, and C. Zhu, “Shaking Table Study on the Seismic Performance of Geogrid Reinforced Soil Retaining Walls,” *Adv. Civ. Eng.*, vol. 2021, no. 1, p. 6668713, 2021, doi: 10.1155/2021/6668713.

[31] C. Zhu, X. Cai, Y. Li, S. Li, X. Huang, and H. Xu, “Study of the performance of a 3D modular geosynthetic reinforced soil bridge abutment under overloading,” *Transp. Geotech.*, vol. 50, p. 101451, Nov. 2024, doi: 10.1016/j.trgeo.2024.101451.

[32] W. Ahmad and T. Uchimura, “The Effect of Moisture Content at Compaction and Grain Size Distribution on the Shear Strength of Unsaturated Soils,” *Sustainability*, vol. 15, no. 6, p. 5123, Mar. 2023, doi: 10.3390/su15065123.

[33] H. Eteraf, B. Kovacs, V. Mikita, and Z. Delshad, “Effect of particle size distribution on shear strength of soil,” *MATEC Web Conf.*, vol. 385, p. 01043, 2023, doi: 10.1051/matecconf/202338501043.

[34] H. Guo *et al.*, “Effect of grain size distribution on the shear properties of sand,” *Frontiers in Materials, vol. 10*, June 2023, doi: 10.3389/fmats.2023.1219765.

[35] H. A. Oravec, V. M. Asnani, C. M. Creager, and S. J. Moreland, “Geotechnical Review of Existing Mars Soil Simulants for Surface Mobility,” presented at the ASCE Earth & Space Conference, Virtual. [Online]. Available: https://ntrs.nasa.gov/api/citations/20200003046/downloads/20200003046.pdf (Accessed July. 11, 2025)

[36] X. Zeng *et al.*, “JMSS-1: a new Martian soil simulant,” *Earth Planets Space*, vol. 67, no. 1, p. 72, Dec. 2015, doi: 10.1186/s40623-015-0248-5.

[37] M. Adams, J. Nicks, T. Stabile, J. T. Wu, W. Schlatter, and J. Hartmann, “Geosynthetic reinforced soil integrated bridge system, synthesis report,” United States. Federal Highway Administration, 2011.

Appendix. Supplementary Figures

Fig. A1. Four layers of glass-fibre geogrid demonstrating sufficient capacity to support the weight of a *Homo sapiens* subject.

Declaration of Academic Integrity

The participating team declares that the paper submitted is comprised of original research and results obtained under the guidance of the instructor. To the team's best knowledge, the paper does not contain research results, published or not, from a person who is not a team member, except for the content listed in the references and the acknowledgment. If there is any misinformation, we are willing to take all the related responsibilities.

Names of team members: Melvin Qiu

Signatures of team members:

Name of the instructor: Siming Huang

Signature of the instructor: Siming Huang

Date: August 23, 2025